Document en libre accès dans PolyPublie
Open Access document in PolyPublie

Document publié chez l'éditeur officiel
Document issued by the official publisher

An efficient multi-scale computation of the macroscopic coefficient of thermal expansion: application to the Resin Transfer Molding manufactured 3D woven composites

Anton Trofimov[a,], Jeremy Le-Pavic[b], Daniel Therriault[a], Martin Lévesque[a]

[a] *Laboratory for Multiscale Mechanics, Polytechnique Montréal, Montréal, QC H3C3A7, Canada*
[b] *Safran Composites, a technology platform of Safran Tech, Itteville, 91760, France*

Abstract

This paper presents a simple and computationally efficient multi-scale procedure to predict the macroscopic temperature dependent coefficient of thermal expansion (CTE) of any linearly thermoelastic material from isothermal mechanical simulations only. The approach relies on Levin's demonstration that, in analytical homogenization, the effective coefficient of thermal expansion is related to the local coefficient of thermal expansion and the stress concentration tensor. For demonstration purposes, this procedure was applied to a 3D woven composite material. The proposed approach was successfully validated with full thermal simulations.

Keywords: multi-scale modeling, homogenization, coefficient of thermal expansion, 3D woven composite

1. Introduction

The Resin Transfer Molding (RTM) process consists in impregnating a dry fiber preform with a thermoset resin and subsequently curing it until its full consolidation. The process involves significant temperature variations that induce residual stresses buildup that may lead to matrix cracking, delamination and/or part distortion Michaud et al. (1998); Corden et al. (1998); Ruiz and Trochu (2005). Residual stresses mainly result from the dissimilar fibers and matrix coefficients of thermal expansion, the polymer cure shrinkage and tool-part interaction Kim and Hahn (1989); Radford and Diefendorf (1993); Radford and Rennick (2000); Wisnom et al. (2006).

The structure of a 3D woven composite is hierarchical with properties varying through the hierarchy of scales. At the meso-scale, the structure is made of tows that are classified as warp

---

(longitudinal) and weft (transverse), and of a polymer matrix. At the micro-scale, the tows are assumed to be made of carbon fibers and the polymer matrix. Properties variation at any scale impact the overall part performance.

The prediction of the macroscopic properties of 3D woven composites during manufacturing requires accurate constitutive theories for the polymer matrix and an efficient multi-scale procedure Boisse (2015); Vasiliev and Morozov (2007). The numerical multi-scale homogenization technique is usually used to compute macroscopic properties by spatially averaging local stresses and strains fields at the micro- and meso-scales Gusev (1997); Segurado and Llorca (2002); González and LLorca (2007). The technique is computationally expensive and requires the generation of volume elements (VEs) representing the micro- or meso-structure. VEs can be constructed artificially to represent the microstructures Widom (1966); Finney (1976); He et al. (1999); Drach et al. (2016) or generated from material images taken by Computed Microtomography (μCT) Stig and Hallström (2012); Yang et al. (2017); Trofimov et al. (2018). External isothermal loads are usually applied to compute the local stress and strain fields in the VE to obtain mechanical properties. Additional sets of thermal loadings are applied to the VE and the homogenization procedure is repeated to predict the coefficient of thermal expansion (CTE) Pierard et al. (2004); Khan and Muliana (2010).

To the best of our knowledge, there is no published work combining all the required steps of a multi-scale procedure to compute the overall CTE of a 3D woven composite from isothermal mechanical simulations alone. The existence of such a procedure would considerably reduce the computational time required to predict composites behaviour throughout the RTM process.

This paper presents a relatively simple and computationally efficient multi-scale procedure to predict the macroscopic temperature dependent CTE of a 3D woven composite from isothermal mechanical simulations alone. Although the procedure is applied to a 3D woven composite, it is of sufficient generality to be applied to any composite. The paper is organized as follows: Section 2 recalls background information on the concept of numerical homogenization for the computation of the effective thermomehcanical properties and details the analytical approach to obtain the CTE from isothermal stress simulations. Section 3 provides the analytical formula to extract the macroscopic CTE from isothermal strain simulations. Section 4 presents the properties of the materials used in this paper. Section 5 details the multi-scale procedure to compute the macroscopic CTE from isothermal simulations. The components of the computed CTEs at each stage of the procedure are presented in Section 6. Final conclusions are given in Section 7.

The modified Voigt notation has been adopted throughout the paper. Symmetric second-order tensors are expressed as six component vectors and symmetric fourth-order tensors are expressed as 6×6 matrices. Scalar quantities are denoted by light-faced letters (i.e., a, α and A), second order tensors are represented by boldfaced lowercase Greek letters (i.e., $\boldsymbol{\sigma}$), while fourth-order tensors are represented by boldfaced capital Roman letters (i.e., $\mathbf{C}$).

Note that all the values of the Young's moduli and the CTEs are normalized by their values of the pure polymer at room temperature, for confidentiality reasons.

2. Background

2.1. Numerical homogenization

The homogenization procedure relies on the concept of Representative Volume Element (RVE) introduced by Hill (1963) who postulated that the VE is equivalent to the RVE when it (i) is a volume large enough to be statistically representative of a heterogeneous material; (ii) possess a constitutive response which is independent with respect to the applied boundary conditions.

The macroscopic constitutive behavior is called *effective* when the RVE is used and is written as Hill (1963); Kröner (1971):

$$\langle \boldsymbol{\sigma} \rangle = \mathbf{C}^{eff} : \left(\langle \boldsymbol{\varepsilon} \rangle - \boldsymbol{\alpha}^{eff} \Delta T \right) \tag{1a}$$

$$\langle \boldsymbol{\varepsilon} \rangle = \mathbf{S}^{eff} : \langle \boldsymbol{\sigma} \rangle + \boldsymbol{\alpha}^{eff} \Delta T, \tag{1b}$$

where $\langle \cdots \rangle$ represents volume averaging, $\mathbf{C}^{eff}$ and $\mathbf{S}^{eff}$ are the effective stiffness and compliance tensors, $\boldsymbol{\alpha}^{eff}$ is the effective CTE, ΔT is a temperature change, $\boldsymbol{\sigma}$ and $\boldsymbol{\varepsilon}$ are the stress and the strain fields inside the RVE, respectively.

Authors in Gusev (1997); Terada et al. (2000) concluded that the periodic boundary conditions (PBC) provide a computationally optimal choice among the other Boundary Conditions (BCs) when the periodic structure is admissible since it requires the minimal volume element to be qualified as RVE. Details on the boundary conditions are given in Appendix A.

Computation of the effective stiffness tensor

A set of six isothermal ($\Delta T = 0$) strain loadcases is usually applied (three uniaxial tension and three shear) to compute the effective elastic stiffness tensor using PBC Segurado and Llorca (2002). From the output of the mechanical simulations, the numerical homogenization procedure is used

to compute the effective stiffness tensor where the homogenized stress components are obtained through spatial averaging as per:

$$\langle \sigma_i \rangle_m = \frac{1}{V} \sum_{l=1}^{M} \left(\sigma_i^{(l)} \right)_m, (i, m = 1, 2, 3, 4, 5, 6),$$ (2)

where $\langle \sigma_i \rangle_m$ is the volume average of the stress component i resulting from the application of the m-th loadcase, V is the total volume of the RVE, $\left(\sigma_i^{(l)} \right)_m$ is the i stress component at the centroid of the finite element l computed from the m-th loadcase, $V^{(l)}$ is the volume of the element l and M is the total number of elements in the model. Given the average stress components and applied strain, the effective stiffness tensor can be computed from Hooke's law $\langle \sigma_i \rangle_m = C_{ij}^{eff} \varepsilon_j^0$, (summation over $j = 1, 2, 3, 4, 5, 6$), where ε^0 is the applied load case.

Computation of the effective CTE tensor

Authors in Karch (2014) applied a uniform temperature change ΔT while the surfaces of the RVE were assumed traction free and the nodes on the opposite faces of the RVE were coupled ensuring periodicity to compute the effective CTE. The strain tensor was averaged as:

$$\langle \varepsilon_i \rangle_m = \frac{1}{V} \sum_{l=1}^{M} \left(\varepsilon_i^{(l)} \right)_m, (i, m = 1, 2, 3, 4, 5, 6),$$ (3)

where $\langle \varepsilon_i \rangle$ is the volume average of the strain component i resulting from the application of the thermal loadcase, $\varepsilon_i^{(l)}$ is the i strain component at the centroid of the finite element l computed from the thermal loadcase. The average stress in the RVE was zero due to the traction free boundary conditions and the effective CTE was straightforwardly obtained from Equation 1b.

The two previous section demonstrate that authors relied on two homogenization simulation steps to compute the effective thermomechanical properties of composites.

2.2. Computation of the effective CTE from isothermal stress load

Levin (1967) showed that the effective CTE of a heterogeneous material having non-uniform CTEs in the inhomogeneities can be directly computed from the mechanical (isothermal) problem using the stress concentration tensor as:

$$\boldsymbol{\alpha}^{eff} = \frac{1}{V} \int_V \boldsymbol{\alpha}(\boldsymbol{x}) : \mathbf{B}(\boldsymbol{x}) \mathrm{d}V,$$ (4)

4

where V is the volume of a RVE, $\boldsymbol{x}$ is the position vector, $\boldsymbol{\alpha}(\boldsymbol{x})$ is the spatially dependent second order CTE tensor, $\mathbf{B}(\boldsymbol{x})$ is the spatially dependent fourth order stress concentration tensor that relates the applied stress $\boldsymbol{\sigma}^0$ to the spatially dependent stress $\boldsymbol{\sigma}(\boldsymbol{x})$ as:

$$\boldsymbol{\sigma}(\boldsymbol{x}) = \mathbf{B}(\boldsymbol{x}) : \boldsymbol{\sigma}^0. \tag{5}$$

Equations (4) and (5) suggest that once $\boldsymbol{\sigma}^0$, $\boldsymbol{\sigma}(\boldsymbol{x})$ and $\boldsymbol{\alpha}(\boldsymbol{x})$ are known, so is $\boldsymbol{\alpha}^{eff}$. Our procedure relies on this key result.

Homogenization relying on the PBCs impose a strain loading and can be used to compute the spatially dependent strain localization tensor $\mathbf{A}(\boldsymbol{x})$. The strain localization tensor relates an applied strain $\boldsymbol{\varepsilon}^0$ to the spatially dependent strain $\boldsymbol{\varepsilon}(\boldsymbol{x})$ inside V such that:

$$\boldsymbol{\varepsilon}(\boldsymbol{x}) = \mathbf{A}(\boldsymbol{x}) : \boldsymbol{\varepsilon}^0. \tag{6}$$

The stress and strain localization tensors are interrelated trough Aboudi et al. (2013):

$$\mathbf{B}(\boldsymbol{x}) = \mathbf{C}(\boldsymbol{x}) : \mathbf{A}(\boldsymbol{x}) : \left(\mathbf{C}^{eff} \right)^{-1}, \tag{7}$$

where $\mathbf{C}(\boldsymbol{x})$ is the spatially dependent stiffness tensor of the material and $\mathbf{C}^{eff}$ is the effective stiffness tensor of the heterogeneous material computed using isothermal simulation.

3. Computation of the effective CTE from isothermal strain load

From Equations (4) and (7), it follows that the effective CTE can be computed as:

$$\boldsymbol{\alpha}^{eff} = \frac{1}{V} \int_V \boldsymbol{\alpha}(\boldsymbol{x}) : \left[\mathbf{C}(\boldsymbol{x}) : \mathbf{A}(\boldsymbol{x}) : \left(\mathbf{C}^{eff} \right)^{-1} \right] dV. \tag{8}$$

In the case of multi-phase composites when the CTE in the k-th phase is uniform, Equation (8) reduces to:

$$\boldsymbol{\alpha}^{eff} = \sum_{k=1}^{N} \phi^{(k)} \boldsymbol{\alpha}^{(k)} : \left[\mathbf{C}^{(k)} : \mathbf{A}^{(k)} : \left(\mathbf{C}^{eff} \right)^{-1} \right], \tag{9}$$

where N is the number of phases, $\phi^{(k)}$ is the volume fraction of k-th phase, $\mathbf{C}^{(k)}$ is the stiffness tensor of k-th phase, $\mathbf{A}^{(k)}$ is the k-th phase volume averaged strain localization tensor and $\boldsymbol{\alpha}^{(k)}$ is the CTE of the k-th phase.

Table 1: Normalized properties of the epoxy matrix at different temperatures.

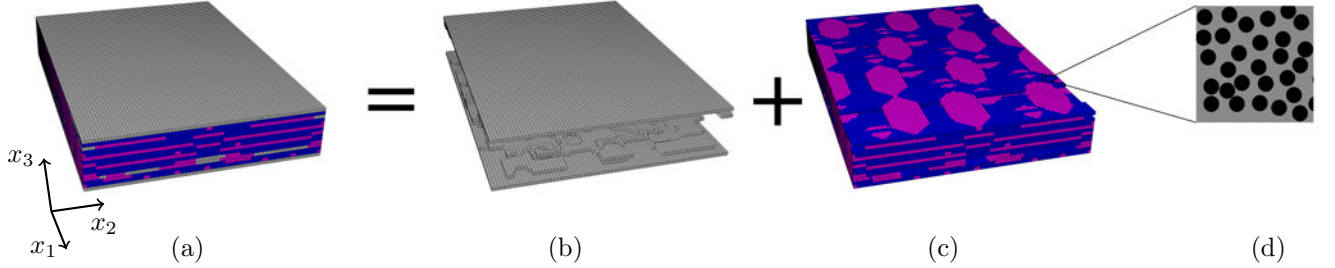| Temperature °C	Young's modulus, E	Poisson's ratio, ν	Coefficient of thermal expansion, α
30	1		1
45	0.997		1
60	0.978		1
75	0.924		1
90	0.864		1
105	0.791	0.39	1
120	0.682		1
135	0.543		1
150	0.357		1
165	0.075		2.986
180	0.009		2.986

Figure 1: The structure of considered 3D woven composite material: (a) composite RVE; (b) polymer matrix; (c) tows; (d) a zoom view of the tows consisting of carbon fibers in a polymer matrix

Using Equation (9), one can obtain the effective CTE directly from the computation of the effective elastic properties and disregard additional thermal simulations, thus, reducing the computational burdent.

4. Materials

Figure 1 illustrates the structure of the considered 3D woven composite. The 3D woven composite consisted of a commercial DGEBF (DiGlycidyl Ether of Bisphenol F) epoxy matrix and tows. The tows are composed of DGEBF epoxy matrix and the carbon fibers. The carbon fibers were assumed to be linearly elastic and transversely isotropic ($E_1 = E_2 = 10\ 300$ MPa, $E_3 = 276\ 000$ MPa;

$\nu_{12} = 0.3$, $\nu_{23} = \nu_{31} = 0.0097$; $G_{12} = 3\,960$ MPa, $G_{23} = G_{31} = 27\,900$ MPa, $\alpha_1 = \alpha_2 = 3.8 \cdot 10^{-6}$ $1/°C$, $\alpha_3 = -0.7 \cdot 10^{-6}$ $1/°C$). The epoxy matrix was assumed to be linearly thermoelastic and isotropic, with properties taken from Courtois et al. (2018); Trofimov et al. (2020). Note that in the works of Courtois et al. (2018); Trofimov et al. (2020), the Poisson's ratio was fixed to 0.39 and the authors measured the linearly viscoelastic response of the polymer with different degrees of cure. In our work, we used the data for the fully cured polymer and considered its instantaneous response. The normalized thermoelastic properties of the epoxy matrix are given in Table 1.

5. Multi-scale procedure to compute the macroscopic CTE of 3D woven composite

We followed a multi-scale procedure to predict the macroscopic CTE of the 3D woven composite from the isothermal simulations. The isothermal loadings at each step were implemented using PBC. The multi-scale procedure starts with the homogenization of the tow's temperature dependent CTEs at the micro-scale using the output from isothermal loadings and Equation (9). The obtained temperature dependent mechanical and thermal properties of the tows were input into a meso-scale RVE where the tows and matrix were explicitly represented. Another round of homogenization procedure from the isothermal simulations and Equation (8) was performed to obtain macroscopic temperature dependent CTEs of the 3D woven composite. The following subsections detail these procedures.

5.1. Computation of the effective CTE of the tows

The tows packing was assumed to be hexagonal in warp and weft directions containing 70% and 75% of carbon fibers, respectively. Figure 2 shows the generated periodic RVE in ABAQUS 6.14.

The PBC consisting of a set of six isothermal unit strain load cases were applied to compute the effective mechanical properties ($\mathbf{C}^{eff}$).

We first averaged the strain field inside the reinforcement phase "1" using Equation (3) to compute the averaged strain localization tensors. Given the average strain components and known applied strain, the averaged strain localization tensor inside the reinforcement phase was computed as:

$$\langle \boldsymbol{\varepsilon}_i^{(1)}(\boldsymbol{x}) \rangle_m = A_{ij}^{(1)} \varepsilon_j^0, \text{ (summation over } j = 1, 2, 3, 4, 5, 6). \tag{10}$$

The averaged strain localization tensor inside the polymer matrix phase "0" was obtained as:
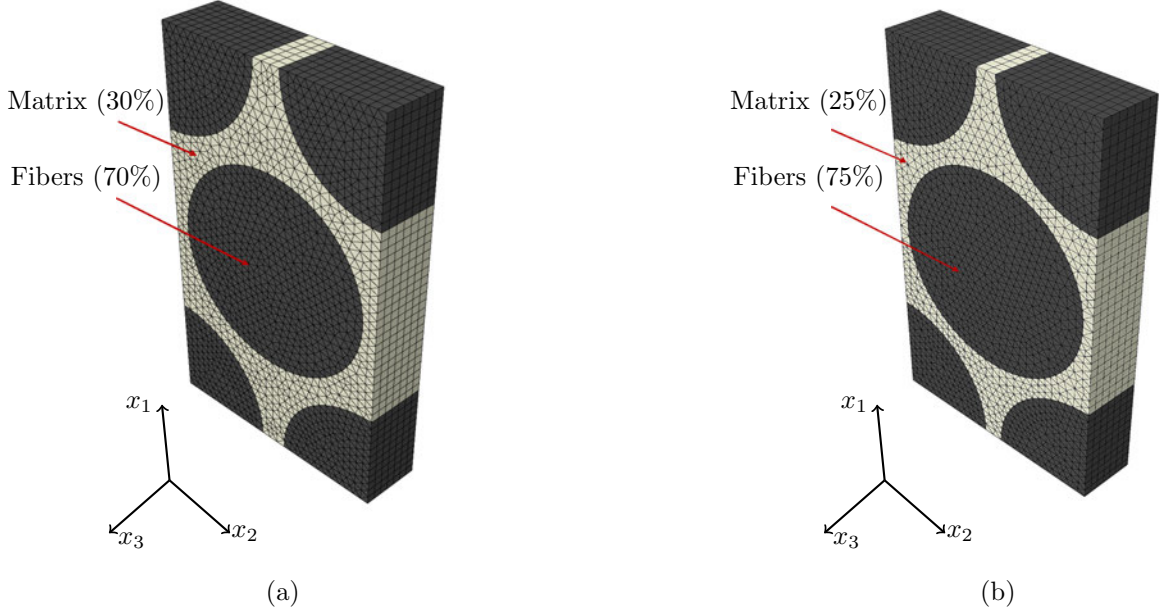
Figure 2: Example of micro-scale RVEs meshed with 4 124 6-node linear triangular prism elements exhibiting carbon fibers volume fractions of: (a) 70% corresponding to the warp tow; (b) 75% corresponding to the weft tow
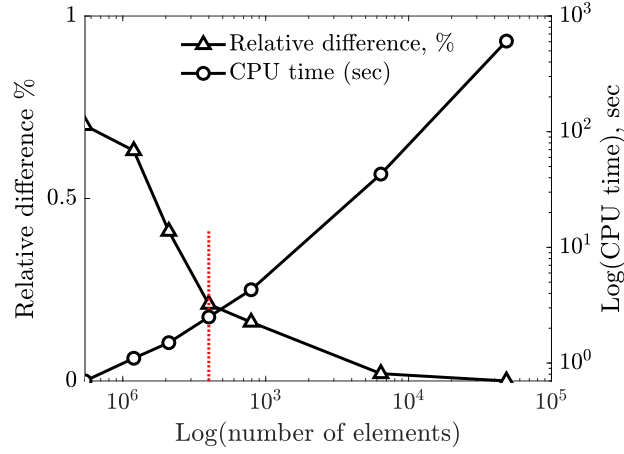

Figure 3: Mesh convergence study for the micro-scale homogenization. Relative difference (%), between the C_{11}^{eff}s and the finest mesh response, and total CPU time are plotted as a function of the number of elements. The chosen mesh is emphasized by a dashed line.

$$\mathbf{A}^{(0)} = \mathbf{I} - \mathbf{A}^{(1)}, \tag{11}$$

where $\mathbf{I}$ is the fourth order identity tensor.

Given the effective stiffness and the averaged strain localization tensors, CTEs and volume fractions of each phase, we computed the effective CTE using Equation (9).
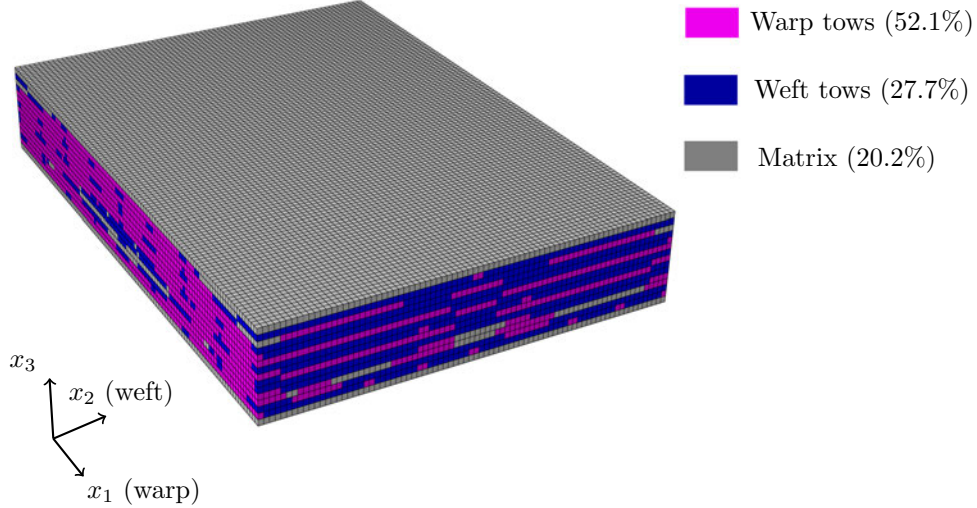
8

Figure 4: Example of the numerical RVE for the whole composite featuring 105 138 linear 8-node brick elements

A convergence analysis based on the computed effective stiffness tensor was performed to identify the optimal number of elements. Figure 3 shows the total CPU time and the relative difference between the C_{11}^{eff} for different numbers of elements and the finest mesh response. The chosen mesh is highlighted by a dashed line and convergence was assumed for all the other components of the stiffness tensors and both types of tows. As a result, 4 124 6-node linear triangular prism elements were used in the mesh.

We simulated the response at temperatures ranging from 30°C to 180°C. To verify our predictions, we performed additional full thermal simulations following the procedure detailed in Section 2.1 at the temperatures used for the isothermal analyses.

5.2. Computation of the macroscopic CTE of the ply

Figure 4 shows the 3D woven RVE architecture constructed with WiseTex Verpoest and Lomov (2005). Weft tows, warp tows and the matrix accounted for 27.7%, 52.1%, 20.2% of the whole volume, respectively. The polymer was assumed to obey linearly thermoelastic properties described in Section 4 and tows' constitutive behaviors were computed in Section 5.1.

The local coordinate system of the tows was defined using three vectors and depicted in Figure 5. The first vector was along the central line of the tow, the second vector was tangent to the tow's cross-section and the third vector was defined as the cross product of the first two.

Similar to the tow's simulations, PBC consisting of a set of six isothermal unit strain load cases were applied to compute the effective elastic properties. From the output of the mechanical
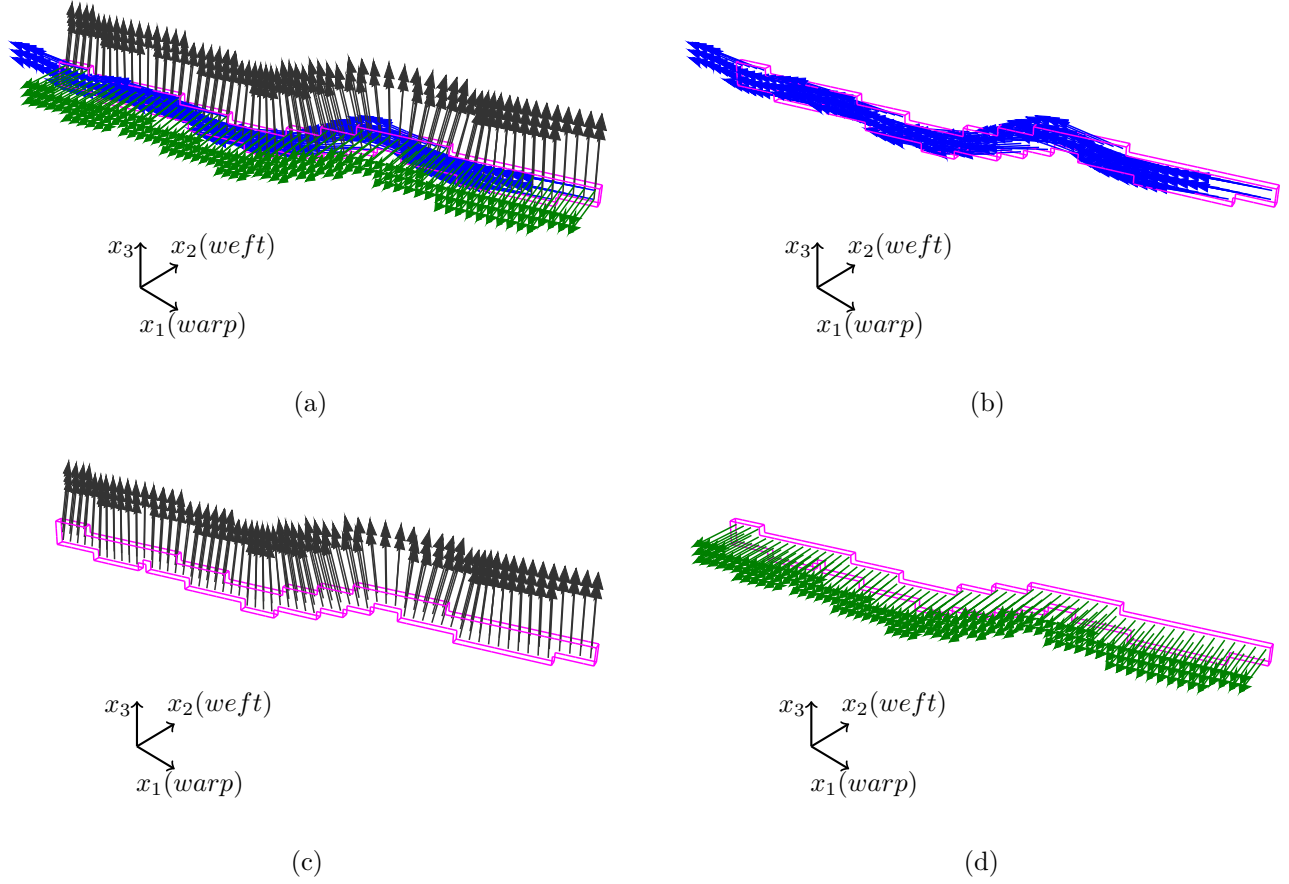
Figure 5: Example of the local coordinate system of a warp tow: (a) all three vectors that described the local coordinate system; (b) the first vector that was along the tow's central line; (c) the second vector that was tangent to the tow's cross-section; (d) the third vector that was as a cross product of the first two.

simulations, the effective CTEs were computed using Equation (8) since the local orientation of the tows produced the non-constant CTE fields with respect to the global coordinate system.

We first computed the effective stiffness tensor of the RVE using the numerical homogenization technique presented in Section 2.1. Next, since we used the unit strain load $\boldsymbol{\varepsilon}^0$, the product of the spatially dependent stiffness obtained in Section 5.1 and strain localization tensors can be computed using the FE output of the spatially dependent stress $\boldsymbol{\sigma}(\boldsymbol{x})$ in the global coordinate system as per:

$$C_{mf}(\boldsymbol{x}) : A_{fi}(\boldsymbol{x}) = \Big(\sigma_i(\boldsymbol{x})\Big)_m, \ \ (i, f, m = 1, 2, 3, 4, 5, 6), \tag{12}$$

where $\Big(\sigma_i(\boldsymbol{x})\Big)_m$ is the stress component i resulting from the application of the m-th loadcase.

The global CTE $\Big(\boldsymbol{\alpha}(\boldsymbol{x})\Big)$ used in Equation 8 was computed from the local CTE $\Big(\boldsymbol{\alpha}^{local}\Big)$ as per:

$$\boldsymbol{\alpha}(\boldsymbol{x}) = \boldsymbol{r}(\boldsymbol{x}) \cdot \boldsymbol{\alpha}^{local}(\boldsymbol{x}) \cdot \boldsymbol{r}^T(\boldsymbol{x}) \tag{13}$$
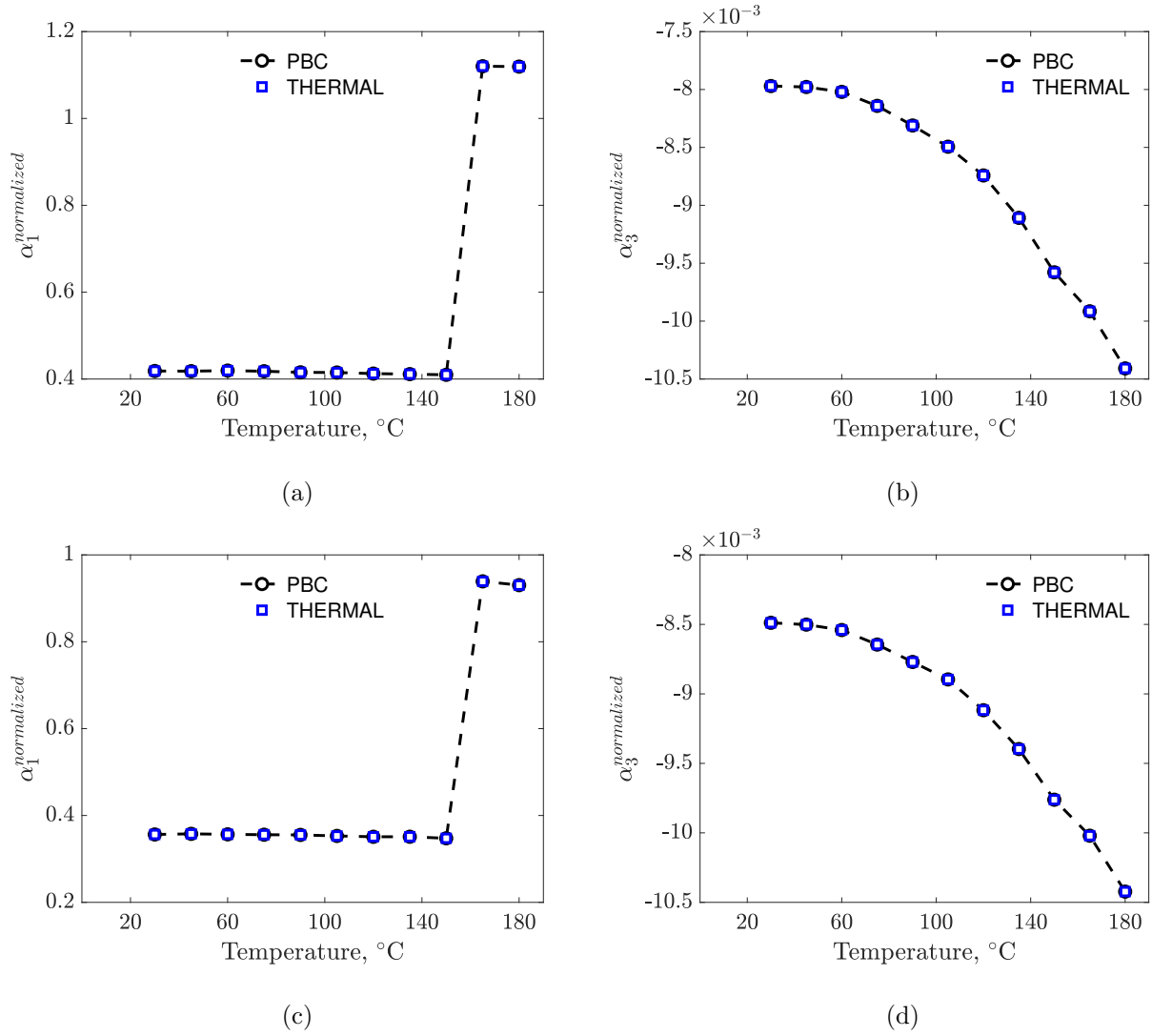
10

Figure 6: Components of the tows effective CTE computed from isothermal (PBC) and thermal loadings (THERMAL): (a) warp tow α_1; (b) warp tow α_3; (c) weft tow α_1 and (d) weft tow α_3.

where the spatially dependent rotation matrix $\boldsymbol{r}(\boldsymbol{x})$ was obtained from the local orientation systems depicted in Figure 5.

We simulated the response at temperatures ranging from 30°C to 180°C. We performed additional full thermal simulations following the procedure detailed in Section 2.1 at the temperatures used for the isothermal analysis to verify predictions.

6. Simulation results

6.1. Tows behavior

Figures 6 (a-d) show the independent non-zero components of warp and weft tows' effective CTEs computed from our procedure and full thermal simulations (THERMAL). Note that the overall properties were transversely isotropic so that $\alpha_1=\alpha_2$ and therefore only two components were plotted. The figure shows that our procedure predicts the same response (within round-off error) as that of the full thermal simulation. The maximum absolute difference in CTEs predictions of warp and weft tows was $\sim 16\%$, which was due to the 5% difference in the volume fraction of the carbon fibers in tows.

In addition, Figures 6 (a-d) show significant variation of the computed effective CTEs with respect to the temperature. This situation can be explained by the evolution of the polymer's thermal and mechanical properties with temperature. It can be seen that the change in the polymer's CTE after the glass transition temperature (T_g) has a more pronounced effect on α_1 than on α_3. This observation results from the fact that the contribution from the fiber to the effective mechanical properties of the composite along global direction x_3 is much higher than in the other directions and it compensates for the changes in the polymer's CTE.

6.2. Ply behavior

Figures 7 (a-c) show the non-zero components of CTEs computed using the PBC and the THERMAL loads. Note that the overall properties were orthotropic and therefore only three components were plotted. The figure shows that our procedure predicts the same response (within round-off error) as that of the full thermal simulation.

In addition, Figures 7 (a-c) show significant temperature dependence of the computed CTE. This observation can be explained by the evolution of elastic and thermal properties of tows and matrix with respect to the temperature. The CTE component along the warp direction α_1 is the smallest and mostly lower than zero. This behaviour results from the fact that the warp tows have the highest volume fraction in the RVE (52.1%) and have negative values for the CTE component along their path. The component of the effective CTE along the weft direction α_2 is higher than α_1 and lower than α_3 values. This observation results from the fact that the weft tows have the second largest volume fraction in the RVE (27.7%) and negative CTE components along their path. The largest values were obtained for α_3 along the global direction x_3 for which tows have the highest positive values of CTEs.
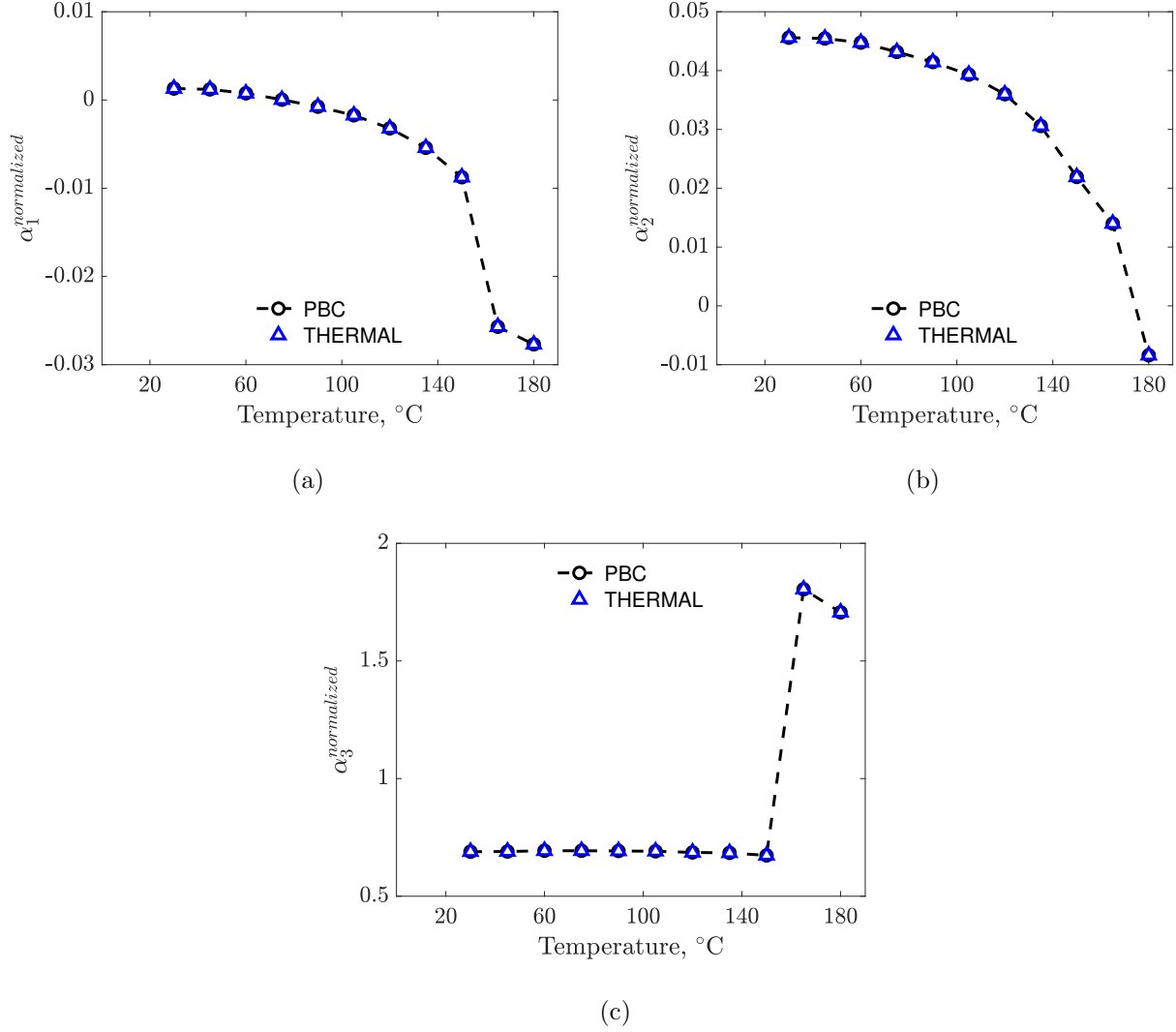
Figure 7: Components of the ply's effective CTE computed from isothermal (PBC) and thermal loadings (THERMAL): (a)α_1; (b)α_2 and (c)α_3.

The change of the polymer's CTE due to the T_g has a stronger influence on the α_3 than on α_1 and α_2 since the RVE is much stiffer along the warp and weft directions, which compensates for this change.

7. Conclusions

This study provided a simple and efficient multi-scale numerical procedure for computing the macroscopic temperature dependent CTE of any linearly thermoelastic material.

The developed procedure computes the effective properties from the isothermal simulations only and therefore reduces the computational efforts related to the additional thermal loadings.

13

Considering that multi-scale simulations are computationally expansive it gives a considerable advantage.

The procedure was successfully validated against the full thermal simulations at all considered temperatures and at each step of multiscale procedure. For demonstration purposes this procedure was applied to the 3D woven composite material.

8. Acknowledgment

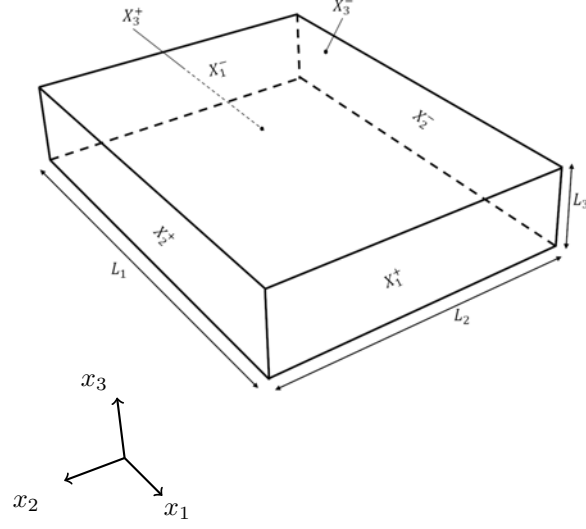# Appendix A. Details on the periodic boundary conditions (PBC)

Figure A1: General geometry of the RVE (L_i the unit cell edges lengths)

Table A1: Prescribed strains corresponding to the six load-cases used for computing the tows effective properties

Prescribed average strain,%	**Load-case**					
	Tensile 1	Tensile 2	Tensile 3	Shear 12	Shear 23	Shear 31
ε_{11}^0	1	0	0	0	0	0
ε_{22}^0	0	1	0	0	0	0
ε_{33}^0	0	0	1	0	0	0
ε_{12}^0	0	0	0	1	0	0
ε_{23}^0	0	0	0	0	1	0
ε_{31}^0	0	0	0	0	0	1

The formulation of the PBC reads:

$$\boldsymbol{u}(\boldsymbol{x})^{(i+)} - \boldsymbol{u}(\boldsymbol{x})^{(i+)} = \boldsymbol{\varepsilon}^0 \cdot \Delta \boldsymbol{x}^i, \tag{A.1}$$

where $\boldsymbol{u}(\boldsymbol{x})^{(i+)}$ is the displacement of the point on the positive surface $i+$, $\boldsymbol{u}(\boldsymbol{x})^{(i-)}$ is the displacement of the point on the negative surface $i+$, $\Delta \boldsymbol{x}^i$ is a constant distance vector between corresponding positive and negative surfaces. Table A1 gives the set of six PBC load cases used for homogenization.

References

Aboudi, J., Arnold, S.M., Bednarcyk, B.A., 2013. Micromechanics of Composite Materials. Elsevier. doi:10.1016/C2011-0-05224-9.

Boisse, P., 2015. Advances in composites manufacturing and process design. Woodhead Publishing.

Corden, T.J., Jones, I.A., Jones, D.T., Middleton, V., 1998. The mechanisms of interlaminar cracking in thick resin transfer moulded composite cylinders. Composites Part A: Applied Science and Manufacturing 29, 455–464. doi:10.1016/S1359-835X(97)00083-3.

Courtois, A., Hirsekorn, M., Benavente, M., Jaillon, A., Marcin, L., Ruiz, E., Lévesque, M., 2018. Viscoelastic behavior of an epoxy resin during cure below the glass transition temperature: Characterization and modeling. Journal of Composite Materials 53, 155–171. doi:10.1177/0021998318781226.

Drach, B., Tsukrov, I., Trofimov, A., 2016. Comparison of full field and single pore approaches to homogenization of linearly elastic materials with pores of regular and irregular shapes. International Journal of Solids and Structures 96, 48–63. doi:10.1016/j.ijsolstr.2016.06.023.

Finney, J.L., 1976. Fine structure in randomly packed, dense clusters of hard spheres. Materials Science and Engineering 23, 199–205. doi:10.1016/0025-5416(76)90194-4.

González, C., LLorca, J., 2007. Mechanical behavior of unidirectional fiber-reinforced polymers under transverse compression: Microscopic mechanisms and modeling. Composites Science and Technology 67, 2795–2806. doi:10.1016/j.compscitech.2007.02.001.

Gusev, A.A., 1997. Representative volume element size for elastic composites: A numerical study. Journal of the Mechanics and Physics of Solids 45, 1449–1459. doi:10.1016/S0022-5096(97)00016-1.

He, D., Ekere, N., Cai, L., 1999. Computer simulation of random packing of unequal particles. Physical Review E 60, 7098–7104. doi:10.1103/PhysRevE.60.7098.

Hill, R., 1963. Elastic Properties of Reinforced Solids: Some Theoritical Principles. doi:10.1016/0022-5096(63)90036-X.

Karch, C., 2014. Micromechanical Analysis of Thermal Expansion Coefficients. Modeling and Numerical Simulation of Material Science 04, 104–118. doi:10.4236/mnsms.2014.43012.

Khan, K.A., Muliana, A.H., 2010. Effective thermal properties of viscoelastic composites having field-dependent constituent properties. Acta Mech 209, 153–178. doi:10.1007/s00707-009-0171-6.

Kim, K.S., Hahn, H.T., 1989. Residual stress development during processing of graphite/epoxy composites. Composites Science and Technology 36, 121–132. doi:10.1016/0266-3538(89)90083-3.

Kröner, E., 1971. Statistical Continuum Mechanics. volume 92 of *CISM International Centre for Mechanical Sciences*. Springer Vienna, Vienna. doi:10.1007/978-3-7091-2862-6.

Levin, V., 1967. On the coefficients of thermal expansion of heterogeneous material. Mekhanika Tverdogo Tela 2, 58–61.

Michaud, D.J., Beris, A.N., Dhurjati, P.S., 1998. Curing behavior of thick-sectioned RTM composites. Journal of Composite Materials 32, 1273–1296. doi:10.1177/002199839803201402.

Pierard, O., Friebel, C., Doghri, I., 2004. Mean-field homogenization of multi-phase thermo-elastic composites: a general framework and its validation. Composites Science and Technology 64, 1587–1603. doi:10.1016/j.compscitech.2003.11.009.

Radford, D., Diefendorf, R., 1993. Shape Instabilities in Composites Resulting from Laminate Anisotropy. Journal of Reinforced Plastics and Composites 12, 58–75. doi:10.1177/073168449301200104.

Radford, D.W., Rennick, T.S., 2000. Separating sources of manufacturing distortion in laminated composites. Journal of Reinforced Plastics and Composites 19, 621–641. doi:10.1106/CRMP-ARE5-GVPP-0Y7N.

Ruiz, E., Trochu, F., 2005. Numerical analysis of cure temperature and internal stresses in thin and thick RTM parts. Composites Part A: Applied Science and Manufacturing 36, 806–826. doi:10.1016/j.compositesa.2004.10.021.

Segurado, J., Llorca, J., 2002. A numerical approximation to the elastic properties of sphere-reinforced composites. Journal of the Mechanics and Physics of Solids 50, 2107–2121. doi:10.1016/S0022-5096(02)00021-2.

Stig, F., Hallström, S., 2012. Spatial modelling of 3D-woven textiles. Composite Structures 94, 1495–1502. doi:10.1016/J.COMPSTRUCT.2011.12.003.

Terada, K., Hori, M., Kyoya, T., Kikuchi, N., 2000. Simulation of the multi-scale convergence in computational homogenization approaches. International Journal of Solids and Structures 37, 2285–2311. doi:10.1016/S0020-7683(98)00341-2.

Trofimov, A., Le-Pavic, J., Ravey, C., Albouy, W., Therriault, D., Lévesque, M., 2020. Multi-scale modeling of distortion in the non-flat 3D woven composite part manufactured using Resin Transfer Molding. Composites Part A: Applied Science and Manufacturing , 106145doi:10.1016/j.compositesa.2020.106145.

Trofimov, A., Mishurova, T., Lanzoni, L., Radi, E., Bruno, G., Sevostianov, I., 2018. Microstructural analysis and mechanical properties of concrete reinforced with polymer short fibers. International Journal of Engineering Science 133, 210–218. doi:10.1016/J.IJENGSCI.2018.09.009.

Vasiliev, V.V., Morozov, E., 2007. Advanced Mechanics of Composite Materials. Elsevier.

Verpoest, I., Lomov, S.V., 2005. Virtual textile composites software WiseTex: Integration with micro-mechanical, permeability and structural analysis. Composites Science and Technology 65, 2563–2574. doi:10.1016/j.compscitech.2005.05.031.

Widom, B., 1966. Random Sequential Addition of Hard Spheres to a Volume. The Journal of Chemical Physics 44, 3888. doi:10.1063/1.1726548.

Wisnom, M., Gigliotti, M., Ersoy, N., Campbell, M., Potter, K., 2006. Mechanisms generating residual stresses and distortion during manufacture of polymer–matrix composite structures. Composites Part A: Applied Science and Manufacturing 37, 522–529. doi:10.1016/j.compositesa.2005.05.019.

Yang, Z., Ren, W., Sharma, R., McDonald, S., Mostafavi, M., Vertyagina, Y., Marrow, T., 2017. In-situ X-ray computed tomography characterisation of 3D fracture evolution and image-based numerical homogenisation of concrete. Cement and Concrete Composites 75, 74–83. doi:10.1016/j.cemconcomp.2016.10.001.